



Power Electronic Systems
Laboratory

© 2011 IEEE

Proceedings of the 8th International Conference on Power Electronics (ECCE Asia 2011), The Shilla Jeju, Korea,
May 30-June 3, 2011.

A Novel Approach for 3D Air Gap Reluctance Calculations

J. Mühlethaler
J.W. Kolar
A. Ecklebe

This material is posted here with permission of the IEEE. Such permission of the IEEE does not in any way imply IEEE endorsement of any of ETH Zurich's products or services. Internal or personal use of this material is permitted. However, permission to reprint/republish this material for advertising or promotional purposes or for creating new collective works for resale or redistribution must be obtained from the IEEE by writing to pubs-permissions@ieee.org. By choosing to view this document, you agree to all provisions of the copyright laws protecting it.



Eidgenössische Technische Hochschule Zürich
Swiss Federal Institute of Technology Zurich

A Novel Approach for 3D Air Gap Reluctance Calculations

J. Mühlethaler*, J. W. Kolar*, and A. Ecklebe†

*Power Electronic Systems Laboratory, ETH Zurich, Email: muehlethaler@lem.ee.ethz.ch

†ABB Switzerland Ltd., Corporate Research, CH-5405 Baden-Dättwil

Abstract—An approach to accurately calculate the reluctance of an air gap is introduced. The approach is easy to handle as it is based on a modular concept where a simple basic geometry is used as a building block to describe different three dimensional air gap shapes. A high degree of accuracy is achieved as the approach is based on an analytical field solution.

Index Terms—Air gap, Reluctance, Permeance

I. INTRODUCTION

A reluctance model of an inductive component enables a fast and straightforward inductance calculation. It also allows one to predict the flux density in each section of the core, thereby making it possible to avoid saturation of the core when designing inductive components. Finally, when calculating winding losses the effect of the air gap fringing flux to the winding losses can be accurately modeled as a function of the Magneto-Motive Force (MMF) across the air gap [1]. The air gap reluctance must be known in advance for an accurate MMF calculation.

The inductance of an inductive component with N winding turns and a total magnetic reluctance $R_{m,tot}$ is calculated as

$$L = \frac{N^2}{R_{m,tot}}. \quad (1)$$

The reluctance of each section of the flux path has to be derived first in order to calculate $R_{m,tot}$. In Fig. 1 such a reluctance model for the example of an E-core is illustrated. The calculation of the reluctance R_{ci} of the core sections is simple: for a core section of length l , cross-section A , and permeability $\mu_r\mu_0$ it is

$$R_{ci} = \frac{l}{\mu_r\mu_0 A}. \quad (2)$$

Problems occur only in the corner sections, however, simple and reasonably accurate approximations for handling these sections exist. The reluctances R_{w1} and R_{w2} represent the flux paths that are not closed over the core and consequently reduces the total magnetic reluctance $R_{m,tot}$. These winding reluctances R_w are rather small and can be neglected in most practical cases. The major relevancy to the inductance value has the air gap reluctance R_g . Unfortunately, it is by far the most difficult to calculate and despite its importance, a simple easy-to-use and accurate approach for calculating the air gap reluctance has not yet been discovered.

Different means of calculating the reluctance of air gaps exist. Under the assumption of a homogenous flux density

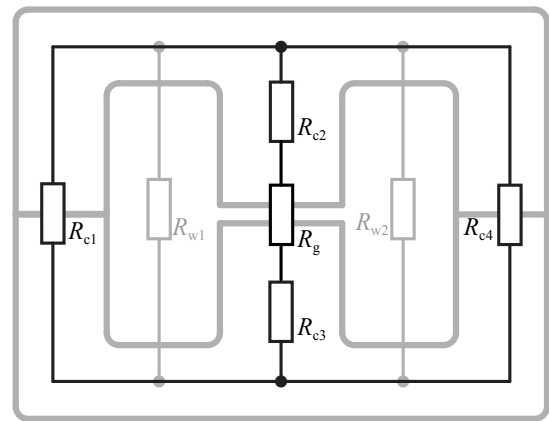


Fig. 1. Illustration of a magnetic reluctance model for the example of an E-core.

distribution in the air gap and no fringing flux, the air gap reluctance can be calculated as

$$R_g = \frac{l_g}{\mu_0 A_g}, \quad (3)$$

where l_g and A_g are the air gap length and air gap cross-section respectively, and μ_0 is the permeability of free space. (3) is only accurate when the fringing flux is small compared to the total flux, as it is when the air gap length is very small compared to the dimension of the air gap cross-section.

Different approaches of how to take the fringing flux into consideration for calculating the air gap reluctance have been derived in the past. The approaches can be basically classified into two categories, which are discussed within the the next two Subsections I-A and I-B.

A. Method of the Conformal Schwarz-Christoffel Transformation

One approach to analytically calculate the reluctance of an air gap geometry is the method of the conformal Schwarz-Christoffel transformation [2]–[4]. The solutions described in [5]–[7] are based on the Schwarz-Christoffel transformation. The approach of [5] is based on the capacitance-to-reluctance analogy to calculate the reluctance of air gaps: if air is the dielectric, the capacitance C can be expressed as

$$C = \epsilon_0 F(g), \quad (4)$$

where $F(g)$ represents the geometry between plates of infinite conductivity and ϵ_0 is the permittivity of free space. The reluctance $R_{m,\text{airgap}}$ of an air gap between surfaces of infinite permeability and having the same geometry $F(g)$ is then

$$R_g = \frac{1}{\mu_0 F(g)}. \quad (5)$$

Hence, calculating the capacitance of the air gap geometry with help of the Schwarz-Christoffel transformation leads directly to the air gap reluctance. However, in [5] only 2D considerations have been made, which considerably limits the practicability of this approach for real 3D air gaps.

Also [6] calculates the magnetic field via the Schwarz-Christoffel transformation, though without the capacitance-to-reluctance analogy. The three-dimensionality of air gaps has been taken into consideration. The solution of approach [6] leads to a relatively complex, difficult to handle, but accurate formula for the air gap reluctance.

B. Increase of the Air Gap Cross-Sectional Area

The fringing flux can be taken into consideration by increasing the actual air gap cross-sectional area (by increasing the air gap cross-sectional area the reluctance is reduced to the actual value) [7]–[9]. According to [8], 10% is a typical value by which the cross-sectional area has to be increased; however, it is admitted that the cross-sectional area should be increased as a function of the air gap length l_g and that a determination of the exact value by which the cross-sectional area has to be increased is difficult. In [9] the reluctance of an air gap with length l_g , width a , and depth d is calculated as

$$R_g = \frac{l_g}{\mu_0(a + l_g)(d + l_g)}. \quad (6)$$

No explanation or derivation of the equation is given. As will be illustrated later, the results deviate from comparison with FEM simulations. In [7] the effective semi-width of the gap, e.g. the radius in case of a round cross-section, is increased by the amount of

$$\left(0.241 + \frac{1}{\pi} \ln \frac{b_a}{l_g}\right) l_g, \quad (7)$$

where b_a is the total inside length of the leg containing the air gap, e.g. for a pot core b_a equals the width of the winding space. No derivation for the formula of (7) is given. However, (7) can be derived from (8)¹ ((8) has not been explained yet but it will be introduced in the next section). This approach is based on the method of the conformal Schwarz-Christoffel transformation and is therefore a hybrid of the two categories. This approach is only capable of calculating the reluctances of air gaps with shapes as illustrated in Fig. 2(a); for this particular air gap shape (air gap type 1/1; cf. next Section) the solution of approach [7] and the solution derived within this paper fit into one another.

$$\frac{1}{l_g} \left[\frac{w}{2l} + \frac{2}{\pi} \left(1 + \ln \frac{\pi h}{4l}\right) \right] \text{ with } l = l_g/2 \text{ and } h = b_a/2 \text{ becomes} \\ \frac{2\mu_0}{l_g} \left[\frac{w}{2} + \frac{l_g}{\pi} \left(1 + \ln \frac{\pi b_a}{4l_g}\right) \right] = \frac{2\mu_0}{l_g} \left[\frac{w}{2} + \left(0.241 + \frac{1}{\pi} \ln \frac{b_a}{l_g}\right) l_g \right].$$

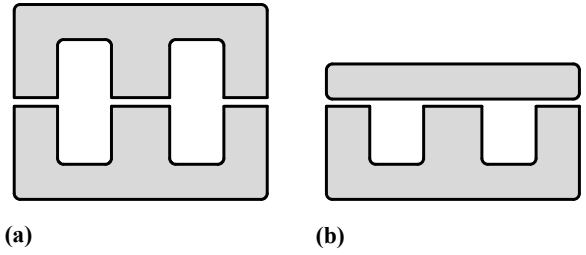


Fig. 2. Illustration of different core shapes that lead to different air gap shapes.

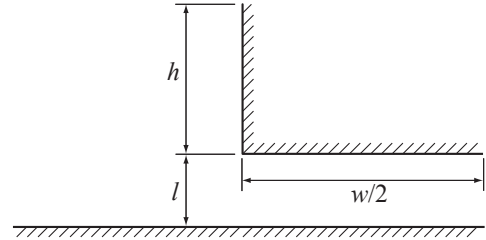


Fig. 3. Basic geometry for air gap calculation.

C. Desired Approach for Air Gap Calculations

Despite its importance, an approach for an air gap calculation that is capable of calculating the reluctance and

- considers the three-dimensionality,
- is reasonable easy-to-handle,
- is capable of handling different shape of air gaps, as e.g. illustrated in Fig. 2,
- while still achieving a high accuracy

has not been found in literature. In particular the need to handle different air gap shapes has, to the author's knowledge, not been covered at all. In the following, a new approach to calculate the air gap reluctance is derived that is very general, easy-to-handle, and considers the three-dimensionality of air gaps. The approach is very accurate because it is based on analytical field solutions.

In Section II the novel approach for air gap calculations is introduced, in Section III equations to calculate reluctances of different core sections are given, and in Section IV reluctance models of E-cores are derived and experimental comparisons are carried out.

II. AIR GAP RELUCTANCE

The novel approach for 3D air gap reluctance calculations is derived from the example of air gaps with square cross-section in Subsection II-A. Later, in Subsection II-B, it is described how to apply the approach to air gaps with round cross-sections.

A. Reluctance of Air Gaps with Square Cross-Section

The reluctance of the simple basic geometry of Fig. 3 is taken as a basis to calculate more complex air gap structures. This basic geometry is used as a building block to describe different three dimensional air gap shapes.

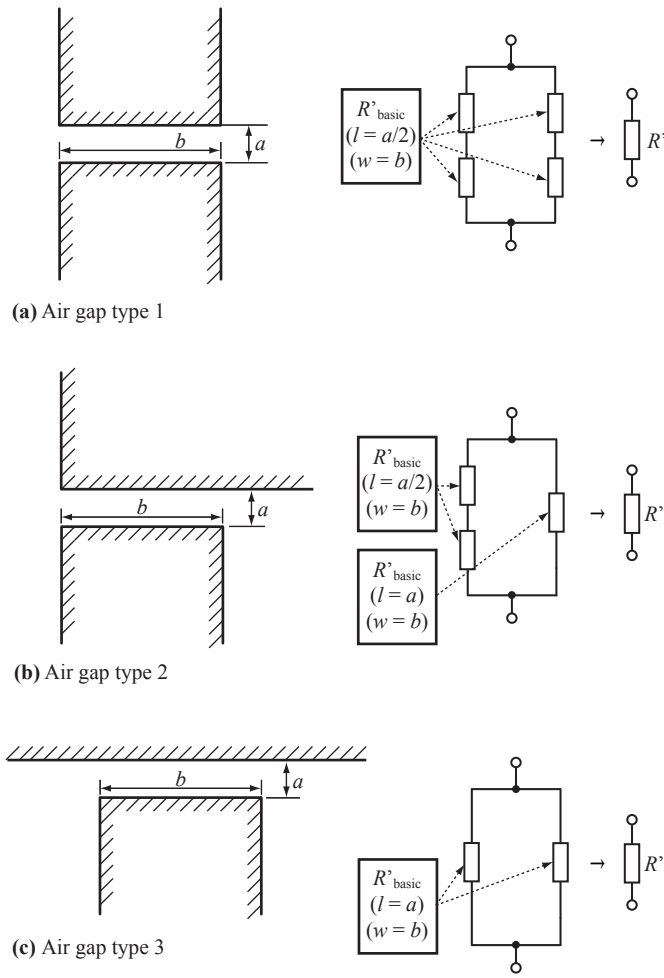


Fig. 4. Different types of air gaps.

The geometry in Fig. 3 has the reluctance per-unit-of-length (2D reluctance)

$$R'_{\text{basic}} = \frac{1}{\mu_0 \left[\frac{w}{2l} + \frac{2}{\pi} \left(1 + \ln \frac{\pi h}{4l} \right) \right]}, \quad (8)$$

where the parameters are as illustrated in Fig. 3. The derivation of (8) has been found in [5] and is given in Appendix A.

Basically, one can think of three types of air gap cross-sections, which are illustrated in Fig. 4. In Fig. 2 two example cores that contain all three air gap types are illustrated. All air gap types can be seen as an assembly of several basic geometries of Fig. 3. Fig. 4 shows how to put together basic geometries to achieve the designated air gap type. In addition it shows how to set the values for w and l of (8). The value h represents the distance from the air gap edge to the next core corner, as e.g. illustrated in Fig. 8.

In order to consider the three dimensionality of air gaps, a fringing factor is introduced that describes by which factor the air gap reluctance decreases due to fringing flux comparing to the idealized reluctance of (3). This approach is introduced using the example of the air gap illustrated in Fig. 5. Assuming, that the air gap is infinitely long in the x -direction

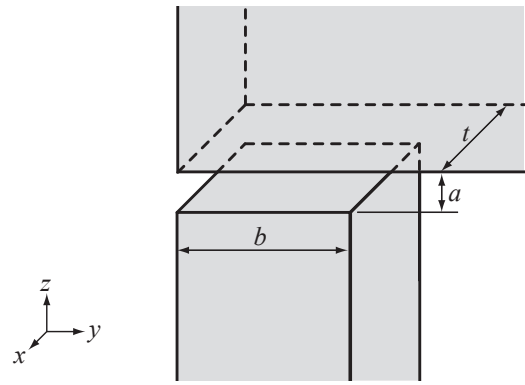


Fig. 5. 3D air gap, based on air gap type 1 (xz -plane) and air gap type 2 (yz -plane) of Fig. 4.

($t \rightarrow \infty$), the fringing effects at the air gap boundaries in the x -direction can be neglected. This air gap has a cross-section as illustrated in Fig. 4(b) (air gap type 2). The fringing factor that considers fringing effects in y -direction is derived by calculating the corresponding air gap reluctance per-unit-of-length R' (as illustrated in Fig. 4(b)) and dividing it by the reluctance per-unit-of-length that neglects any fringing effects (cf. (3)):

$$\sigma_y = \frac{R'}{\frac{a}{\mu_0 b}}. \quad (9)$$

In a similar manner the fringing factor considering fringing effects in the x -direction can also be derived. Assuming an air gap that is infinitely long in the y -direction ($b \rightarrow \infty$), the fringing effects at the air gap boundaries in the y -direction can be neglected. This air gap has a cross-section as illustrated in Fig. 4(a) (air gap type 1). The fringing factor considering fringing effects in the x -direction is derived by calculating the corresponding air gap reluctance per-unit-of-length R' (as illustrated in Fig. 4(a)) and dividing it by the reluctance per-unit-of-length that neglects any fringing effects (cf. (3)):

$$\sigma_x = \frac{R'}{\frac{a}{\mu_0 t}}. \quad (10)$$

The 3D fringing factor is derived by multiplying the two fringing factors σ_x and σ_y

$$\sigma = \sigma_x \sigma_y. \quad (11)$$

The reluctance of the air gap can then be easily calculated with (3) and (11)

$$R_{\text{m,airgap}} = \sigma \frac{a}{\mu_0 \cdot t \cdot b}. \quad (12)$$

The novel approach for reluctance calculations (12) has been compared to the "classical" approach of (3), the approach of (6), and to FEM simulations. The results are given in Fig. 6. The comparisons have been made for a type 1/1 air gap with fixed parameters (leg width and depth: $w = 40$ mm, and distance between air gap and next core corner $h = 40$ mm).

Type 1/2 and type 1/3 air gaps have been compared to FEM simulations as well: the accuracy obtained has always been $\leq 4\%$.

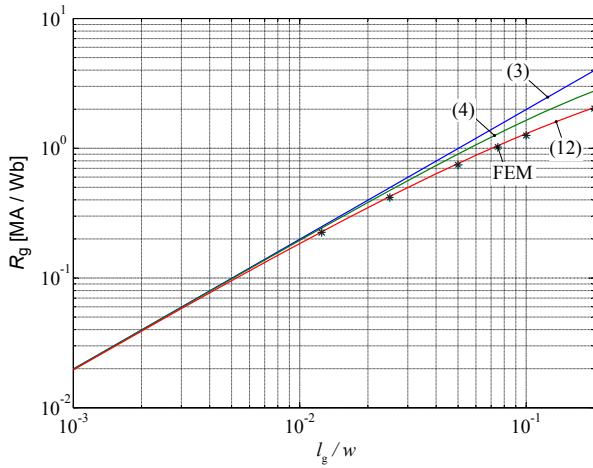


Fig. 6. Comparison of air gap calculation approaches.

B. Reluctance of Air Gap with Round Cross-Section

The fringing factor considering fringing effects in r -direction (polar coordinate system) is

$$\sigma_r = \frac{R'}{\mu_0 r}, \quad (13)$$

where a is the air gap length, r the radius of the air gap, and R' represents the air gap reluctance per-unit-of-length of half of the core leg (including fringing effects). This fringing factor has to be squared as r appears squared in the calculation of the air gap cross-section. As a consequence, the accurate reluctance can be calculated as

$$R_g = \sigma_r^2 \frac{a}{\mu_0 r^2 \pi}. \quad (14)$$

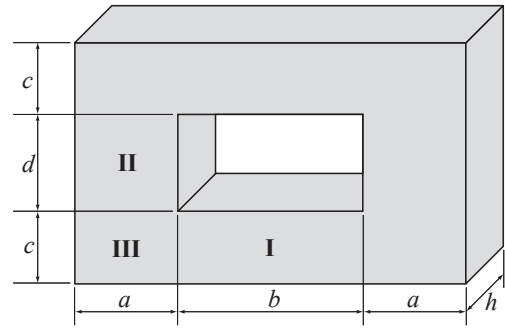
III. CORE RELUCTANCE

In addition to the dominating air gap reluctance the core reluctance has to be calculated to achieve the complete reluctance model. The reluctance of a core section i can be calculated as

$$R_{ci} = \frac{l_i}{\mu_0 \mu_r A_i}, \quad (15)$$

where l_i and A_i are the length and cross-section of section i . Hence, for every section the magnetic path length and the cross-sectional area have to be calculated first. This is difficult for corner sections. Practical cores have usually sharp corners, where the flux tends to concentrate on the inside the bend, so shortening the mean magnetic path. Sophisticated ways of describing A_i and l_i of corner sections exist, e.g. introduced in [6]. However, it is unclear whether the difficult formulas of [6] lead to better results as it neglects the fact that the flux density concentrates mainly at the inner bend. In any case, the corners represent only a minor part of the core. Therefore, for this work the simple approximations of Fig. 7 have been taken.

The accuracy can be further improved by taking the non-linearity of the core material into consideration, i.e. $\mu_r = f(H)$.



Section	l_i	A_i
I	b	ch
II	d	ah
III	$\frac{2\pi}{4} \cdot \frac{(a+c)}{4} = \frac{\pi}{8}(a+c)$	$\frac{h(a+c)}{2}$

Fig. 7. Approximations of core dimensions for core reluctance calculation [7].

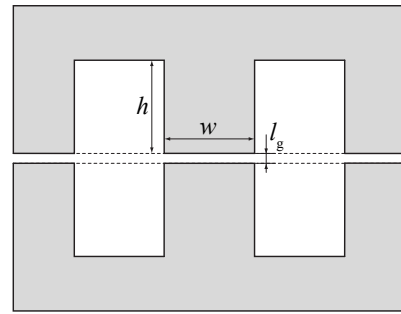


Fig. 8. Built E core for inductance calculation and measurement comparison.

IV. EXPERIMENTAL RESULTS

This Section presents some experimental results that well illustrate the accuracy that can be achieved.

A. Inductance

In Table I measurements and calculated inductance values of an inductor built of two E-Cores (EPCOS ferrite N27; core E55/28/21 [10]; winding turns $N = 80$) are given. The core has three air gaps of length l_g as illustrated in Fig. 8. The inductances for different air gap lengths have been measured. The calculation has been performed with the idealized "classic" approach (3) and the newly derived approach (12). As can be seen, it is not appropriate to neglect the fringing flux; the classic approach leads to an underestimation of the inductance value. The calculation with the newly derived approach leads to accurate results.

B. Saturation

The saturation current I_{sat} is another very important design parameter. A current that is higher than the saturation current would result in a flux density above the saturation flux density B_{sat} . This would result in a substantial decrease of the

TABLE I
MEASUREMENT RESULTS OF E-CORE

Air Gap Length l_g	Calculated classically (3)	Calculated with new approach (12)	Measured
1.0 mm	1.42 mH	1.97 mH	2.07 mH
1.5 mm	0.96 mH	1.47 mH	1.58 mH
2.0 mm	0.72 mH	1.22 mH	1.26 mH

relative permeability μ_r , hence the inductance would drop. The saturation current can be calculated as

$$I_{\text{sat}} = \frac{B_{\text{sat}} A_e N}{L}. \quad (16)$$

TABLE II
MEASUREMENT RESULTS OF E-CORE

	Calculated classically (3)	Calculated with new approach (12)
L	2.75 mH	3.55 mH
I_{sat}	4.6 A	3.6 A

An inductor built of two E-cores with an air gap in the center leg (EPCOS ferrite N27; core E55/28/21 [10]; air gap in the center leg with length $l_g = 1$ mm; winding turns $N = 80$) has been built. In Table II, inductance values and saturation currents are given. The saturation flux density is taken from the data sheet B - H -curve [10] and is approximately $B_{\text{sat}} = 0.45$ T. The results can be compared to a measurement for which the measured current waveform is given in Fig. 9. A rectangular voltage waveform has been applied across the built inductor to achieve this current waveform. The measured saturation current I_{sat} is approximately 3.7 A, which corresponds well to the calculated value.

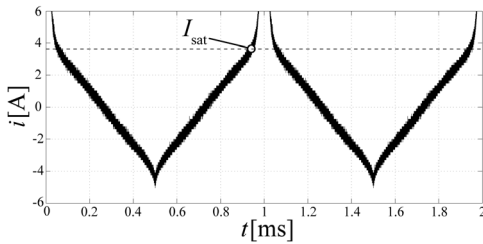


Fig. 9. Measurement of saturation current.

V. CONCLUSION AND FUTURE WORK

An accurate air gap reluctance calculation is essential when designing inductive components. Despite its importance, a simple easy-to-use approach when calculating the air gap reluctance was absent. This paper has shown an approach that is easy-to-handle because of its modular concept (different shapes of air gaps can be built of a simple structure that is easy to calculate), and which still achieves a high level of accuracy as the approach is based on analytical field solutions.

APPENDIX A DERIVATION OF BASIC RELUCTANCE

The derivation of the basic reluctance (8) is given in this section. All considerations are based on works presented in [2], [5], [6]. A function of the type

$$z = f(t) = x(u, v) + jy(u, v) \quad (17)$$

that defines a complex variable $z = x + jy$ as a function of another complex variable $t = u + jv$ and preserves angles is termed conformal. Conformal transformations are very helpful to derive field solutions. A transformation equation must be found relating the given field to a simpler one to which a solution is known or easily found.

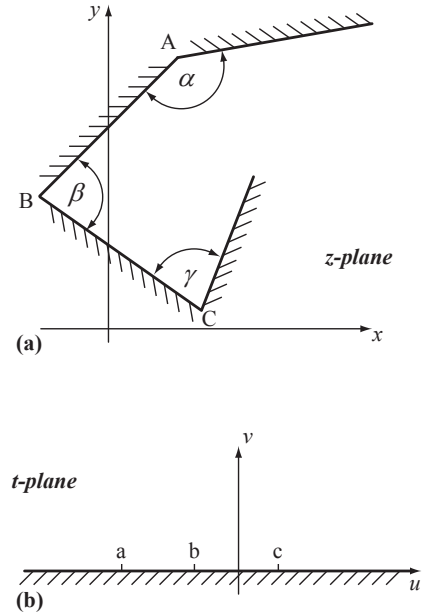


Fig. 10. Illustration of Schwarz-Christoffel Transformation.

One particular conformal transformation equation that transforms the real axis of one plane to the boundary of a polygon of another plane was first given, independently, by Schwarz and Christoffel. The transformation is in such a way that the upper half of the first plane transforms into the interior of the polygon.

For the situation that is illustrated in Fig. 10 the transformation from the real axis of the t -plane to the polygon boundary in the z -plane is derived by integrating the equation

$$\frac{dz}{dt} = S(t-a)^{(\alpha/\pi)-1}(t-b)^{(\beta/\pi)-1}(t-c)^{(\gamma/\pi)-1} \dots, \quad (18)$$

which is named the *Schwarz-Christoffel differential equation*. S is a constant, a, b, c, \dots are points on the real axis in the t -plane corresponding to the points A, B, C, \dots in the z -plane, and $\alpha, \beta, \gamma, \dots$ are the interior angles of the vertices of the polygon in the z -plane.

The Schwarz-Christoffel transformations that are used to calculate the reluctance of the basic geometry of Fig. 3 are

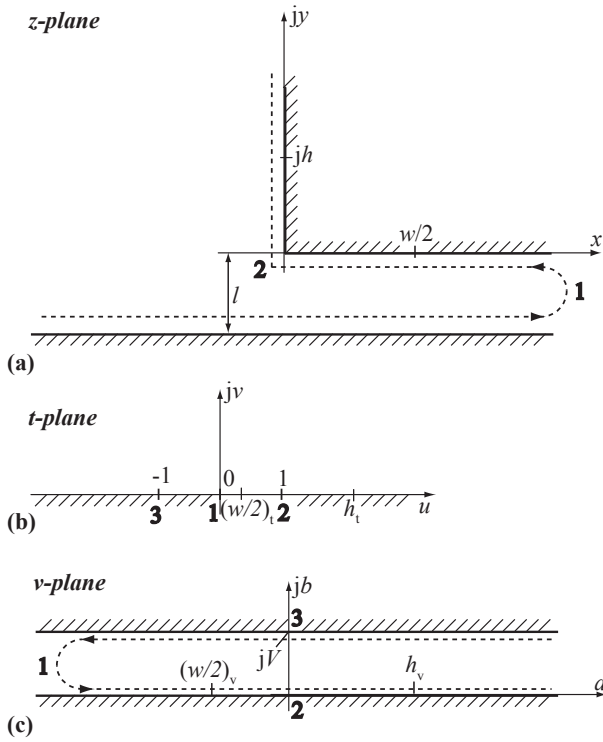


Fig. 11. The Schwarz-Christoffel transformation of the basic geometry.

given in the following. Two transformation equations have to be found: first a transformation equation that relates the basic geometry in the z -plane (cf. Fig. 11(a)) to the real axis in the t -plane (cf. Fig. 11(b)) is derived. Second, a transformation equation that relates the real axis of the t -plane to a geometry of a parallel-type capacitor (cf. Fig. 11(c)) is further derived. The geometry of a parallel-type capacitor permits easy calculation of the capacitance that, with (5), directly leads to the reluctance. The dashed line in Fig. 11(a) illustrates the chosen polygon structure that will be transformed to the real axis in the t -plane of Fig. 11(b). In Table III the vertex coordinates of the z -plane polygon, the vertex angles, and the corresponding points on the real axis of the t -plane are given. This leads to the Schwarz-Christoffel differential equation

$$\frac{dz}{dt} = S_1 t^{-1} (t-1)^{1/2} = S_1 \frac{\sqrt{t-1}}{t}, \quad (19)$$

hence

$$z(t) = -jS_1 (2 \ln(1 + \sqrt{1-t}) - \ln t - 2\sqrt{1-t}) + C_1, \quad (20)$$

where S_1 and C_1 are constants that have to be further determined. Taking $z(1) = 0$, C_1 becomes $C_1 = 0$. Taking $z(t \rightarrow 0) = \infty$ for the second boundary condition some further steps are necessary. Assume $t = \epsilon e^{j\theta}$ and thus $dt = j\epsilon e^{j\theta} d\theta$. For $t \rightarrow 0$, (19) becomes

$$dz = S_1 \frac{j}{t} dt = jS_1 \frac{j\epsilon e^{j\theta} d\theta}{\epsilon e^{j\theta}} = -S_1 d\theta. \quad (21)$$

Near $t = 0$ (point 1 in Fig. 11), z varies from $x - jl$ to x and θ varies from π to zero. Thus,

$$\int_{x-jl}^x dz = - \int_{\pi}^0 S_1 d\theta, \quad (22)$$

hence, $jl = S_1 \pi$ or $S_1 = j \frac{l}{\pi}$. Thus, the transformation equation is fully described

$$z(t) = \frac{l}{\pi} (2 \ln(1 + \sqrt{1-t}) - \ln t - 2\sqrt{1-t}). \quad (23)$$

TABLE III
TRANSFORMATION TABLE 1.

	1	2
z_i	∞	0
α/π	0	3/2
t_i	0	1

The transformation equation relating the real axis of the t -plane to a geometry of a parallel-type capacitor (cf. Fig. 11(c)) will be derived next. The appropriate transformation table is given in Table IV, which leads to the Schwarz-Christoffel differential equation

$$\frac{dv}{dt} = S_2 t^{-1} = \frac{S_2}{t}, \quad (24)$$

hence

$$v(t) = S_2 \ln t + C_2, \quad (25)$$

where S_2 and C_2 are constants that have to be further determined. With $v(1) = 0$, C_2 becomes $C_2 = 0$. With $v(-1) = jV$, where V represents a constant that will cancel out later,

$$jV = S_2 \ln(-1) = S_2 j\pi, \quad (26)$$

hence, $S_2 = V/\pi$. Thus, the transformation equation is described

$$v(t) = \frac{V}{\pi} \ln t. \quad (27)$$

TABLE IV
TRANSFORMATION TABLE 2.

	1
v_i	$-\infty$
α/π	0
t_i	0

For the geometry in Fig. 11(c) the capacitance per unit length can be calculated as

$$C' = \epsilon_0 \frac{h_v - (\frac{w}{2})_v}{V}, \quad (28)$$

where h_v and $(w/2)_v$ have to be determined based on the above derived transformation functions. First, $(w/2)_v$ will be derived. From (23) and with $t \approx 0$

$$\begin{aligned} z(t) = x + j0 &= \frac{l}{\pi} (2 \ln(1 + \sqrt{1-t}) - \ln t - 2\sqrt{1-t}) \\ &= \frac{l}{\pi} (2 \ln 2 - \ln t - 2), \end{aligned} \quad (29)$$

hence,

$$-\ln t = \frac{\pi x}{l} + 2(1 - \ln 2). \quad (30)$$

With (27) and inserting $x = w/2$, $(w/2)_v$ becomes

$$\left(\frac{w}{2}\right)_v = \frac{V}{\pi} \ln t = -\frac{V}{\pi} \left(\frac{\pi w}{2l} + 2(1 - \ln 2)\right). \quad (31)$$

Next, h_v will be derived. From (23) and with $t \rightarrow \infty$

$$\begin{aligned} z(t) &= 0 + jy = \frac{l}{\pi} (2 \ln(1 + \sqrt{1-t}) - \ln t - 2\sqrt{1-t}) \\ &= \frac{l}{\pi} (\ln(-1) + 2j\sqrt{t}), \end{aligned} \quad (32)$$

hence,

$$jy = j \frac{l}{\pi} (\pi + 2\sqrt{t}) \quad (33)$$

or

$$\frac{\pi y}{2l} = \frac{\pi}{2} + \sqrt{t}. \quad (34)$$

Since $t \rightarrow \infty$, (34) can be simplified to

$$\sqrt{t} \approx \frac{\pi y}{2l} \quad (35)$$

and

$$t = \left(\frac{\pi y}{2l}\right)^2 \quad (36)$$

With (27) and inserting $y = h$, h_v becomes

$$h_v = \frac{V}{\pi} \ln t = \frac{2V}{\pi} \ln \frac{\pi h}{2l}. \quad (37)$$

Therewith, the capacitance of the geometry in Fig. 11 is determined. (38) is

$$\begin{aligned} C' &= \epsilon_0 \frac{\frac{2V}{\pi} \ln \frac{\pi h}{2l} + \frac{V}{\pi} \left(\frac{\pi w}{2l} + 2(1 - \ln 2)\right)}{V} \\ &= \epsilon_0 \left[\frac{w}{2l} + \frac{2}{\pi} \left(1 + \ln \frac{\pi h}{2l}\right) \right]. \end{aligned} \quad (38)$$

(5) and (38) lead to the basic reluctance of (8).

ACKNOWLEDGEMENT

The authors would like to thank ABB Switzerland Ltd. for giving them the opportunity to work on this very interesting project.

REFERENCES

- [1] A. V. den Bossche and V. C. Valchev, *Inductors and Transformers for Power Electronics*. CRC Press, Taylor & Francis Group, 2005.
- [2] K. J. Binns, P. J. Lawrenson, and C. W. Trowbridge, *The Analytical and Numerical Solution of Electric and Magnetic Fields*. John Wiley & Sons, Inc., 1992.
- [3] M. Walker, *The Schwarz-Christoffel transformation and its applications - a simple exposition*. Dover Publications, Inc., 1964.
- [4] J. Thomson, *Notes on recent researches in electricity and magnetism*. Oxford, 1893.
- [5] A. Balakrishnan, W. T. Joines, and T. G. Wilson, "Air-gap reluctance and inductance calculations for magnetic circuits using a schwarz-christoffel transformation," *IEEE Transactions on Power Electronics*, vol. 12, pp. 654-663, July 1997.
- [6] P. Wallmeier, *Automatisierte Optimierung von induktiven Bauelementen für Stromrichteranwendungen*. PhD thesis, Universität - Gesamthochschule Paderborn, 2001.
- [7] E. C. Snelling, *Soft Ferrites, Properties and Applications*. 2nd edition, Butterworths, 1988.
- [8] M. K. Kazimierczuk, *High-Frequency Magnetic Components*. A John Wiley and Sons, Ltd., Publication, 2009.
- [9] N. Mohan, T. M. Undeland, and W. P. Robbins, *Power Electronics - Converters, Applications, and Design*. John Wiley & Sons, Inc., 2003.
- [10] *Ferrites and Accessories, Edition 2007*. EPCOS AG.